Building and Environment 188 (2021) 107467

Contents lists available at ScienceDirect

Building and Environment

journal homepage: http://www.elsevier.com/locate/buildenv

Numerical Study of Three Ventilation Strategies in a prefabricated COVID-19 inpatient ward

Juan Ren [a,d,1], Yue Wang [b,1,*], Qibo Liu [a,c], Yu Liu [d]

[a] School of Architecture, Chang'an University, Xi'an, Shaanxi, China
[b] National Key Laboratory of Science and Technology on Aerodynamic Design and Research, School of Aeronautics, Northwestern Polytechnical University, Xi'an, Shaanxi, China
[c] Engineering Research Center of Highway Infrastructure Digitalization, Ministry of Education, Xi'an, Shaanxi, China
[d] School of Mechanics, Civil Engineering and Architecture, Northwestern Polytechnical University, Xi'an, Shaanxi, China

ARTICLE INFO

Keywords:
Ventilation strategy
Prefabricated inpatient ward
COVID-19
CFD

ABSTRACT

Prefabricated inpatient wards have been proven to be an efficient alternative to quickly extend the caring capacity for patients. In this study, three typical ventilation strategies were studied using computational fluid dynamics in a prefabricated Coronavirus disease 2019 double-patient ward. Pollutants are the respiratory droplets and aerosols injected from two manikins. They are modelled as particles with different diameters (3 μm, 6 μm, 12 μm, 20 μm, 45 μm and 175 μm) by the Eulerian–Lagrangian model. Three ventilation strategies with an identical air change rate of 12.3 h^{-1} but different layouts of inlets and outlets are implemented. The flow field, flow structures and particle trajectories have been analysed and compared among the three ventilation strategies. The fate of particles is analysed and compared quantitatively. It is found that small particles (<20 μm) can move along with the main flow streams. Most of them are removed by ventilation to the outlet(s). Large particles (>45 μm) cannot move with the flow streams over a long path. Most of them deposit on solid surfaces in different regions of the ward in each ventilation strategy. Health workers should pay close attention to these polluted areas. Targeted cleaning of the polluted areas is necessary in a prefabricated inpatient ward. To promote the removal of some large particles (e.g., 45 μm) by the outlet(s), the outlet(s) should be installed inside the landing area of large particles and close to the polluted source(s).

1. Introduction

Due to the circumstances of the Coronavirus disease 2019 (COVID-19), prefabricated health care facilities are in urgent need to combat the coronavirus. The modular construction of prefabricated health care facilities demonstrates a high degree of composability and replicability. As a result, it is an efficient alternative to meet patients' emergency needs in COVID-19 outbreak areas. In prefabricated infectious health care facilities, isolation wards are the main therapeutic space. Due to the limited space size of prefabricated wards and strong infectiousness of coronavirus, the ventilation strategy should be carefully designed for prefabricated COVID-19 inpatient wards.

As reported by the World Health Organization on July 9, 2020 [1], coronavirus is primarily transmitted between people through respiratory droplets (>5–10 μm in diameter) and contact routes [2–6]. Some recent publications indicate that COVID-19 may transmit through aerosols (<5 μm in diameter) [7,8]. Both respiratory droplets and aerosols can survive in air for a certain time and move with the air flow for a certain distance. Sufficient evidence has demonstrated the association between ventilation strategies and dissemination of nosocomial pathogens in wards [9]. Since a large number of nurses have been infected while providing health care for COVID-19 patients [10], the ventilation strategy in a COVID-19 isolation ward must reduce the infection risk as much as possible. In addition, providing good ventilation and air quality in a ward is not only critical for inpatients' health but also important for nursing work.

COVID-19 inpatient wards are expected to have better and stricter ventilation strategies than general hospital wards. When patients are coughing or sneezing, the droplets containing pathogens can be sprayed as air jets with velocities greater than 11 m/s [11,12]. These pathogens can spread in the air and deposit on the surface of nursing equipment or

---

[*] Corresponding author.
E-mail address: yuewang@nwpu.edu.cn (Y. Wang).
[1] These authors contributed equally to this work.

https://doi.org/10.1016/j.buildenv.2020.107467
Received 14 July 2020; Received in revised form 10 November 2020; Accepted 12 November 2020

Nomenclature

ACH	Air change per hour
COVID-19	Coronavirus disease 2019
DRW	Discrete random walk
PPE	Personal protective equipment
RMS	Root mean square
d_p	Particle diameter
g	Gravitational acceleration
$\bar{p}$	Reynolds-averaged pressure
$\bar{u}$	Reynolds-averaged velocity
u_p	Particle velocity
ρ	Fluid density
ν	Dynamic viscosity
τ^{RS}	Reynolds stress
F_B	Buoyancy force
F_G	Gravitational force
CFD	Computational fluid dynamics
NS	Navier-Stokes
GAMG	Geometric algebraic multigrid
RANS	Reynolds-averaged Navier-stokes
TKE	Turbulence kinetic energy
$\bar{f}_D$	Additional body forces
m_p	Particle mass
u	Velocity
u'	Fluctuating velocity
x_p	Position vector of the particle
ρ_p	Particle density
ζ	Normally distributed random number
C_D	Drag coefficient
F_D	Drag force
Re_p	Particle Reynolds number

on the floor close to the entrance door. This is very dangerous for the working doctors and nurses. Because of the outbreak of the COVID-19 pandemic, these health workers suffer from a shortage of personal protective equipment (PPE) [13]. Poor ventilation strategies in general hospital wards amplify the infection risk. It is widely assumed that increasing the air change rate (ACH) can reduce the infection risk. However, some researchers have reported that the infection risk could increase with increasing ventilation rates due to an inappropriate ventilation strategy [14,15]. Hence, several studies have emphasized the ventilation strategy as a determinant controlling contaminant flow paths [16–18]. Compared to general hospital wards, COVID-19 inpatient wards have their special requirements of ventilation systems. The COVID-19 inpatient ward should have negative pressure in an isolation room. The minimum air change should be over 12 per hour [19]. The isolation room should be well sealed. The doors should be self-closing. The windows are normally sealed in a prefabricated hospital. The outlets in the ward should have air filtration systems. The ideal ventilation strategy shall supply a mass of fresh air to health care workers and collect pathogens at the outlets in the ward. The pathogens can be collected and well-disposed in the air filtration system.

In the engineering field, the airborne transmission between occupants indoors is usually investigated using both experiments and Computational fluid dynamics (CFD) methods [20]. Experimental methods include quantitative measurement of the concentration field [21,22] and imaging visualization of expiratory flows [11,12]. Chamber experiments using breathing thermal manikins and ancillary machines [23,24] have been the primary method of investigating airborne transmission between occupants and quantifying the risk of cross-infection. In general, chamber experiments can provide reliable results since they take full account of the indoor aerodynamics of real ventilation flows and tracer gas/particles. Liu et al. [25] studied the boundary conditions and flow fields in the first-class cabin of a functional MD-82 commercial airliner. Their results can provide high quality data for validating CFD models. In recent study, Liu et al. [26]developed fast fluid dynamics with the Markov chain method to model the transient particle transport in transient indoor airflow. With this new method, the computational time was 7.8 times less than that of the CFD + Eulerian method. Bolster and Linden [27] focused on transient contaminant transport by modelling three transient contamination scenarios, namely, the so called ‘step-up’, ‘step-down’, and point source cases. They found that, on average, traditional and low-energy systems can be similar in overall pollutant removal efficiency. Zhang et al. [28] injected a large number of newly created nano-particle aggregates into a chamber for the purposes of removing harmful contents in an indoor environment.

With the development of computational techniques, CFD has been increasingly used in the analysis of indoor environments. In CFD simulations, the airflow in a room is generally described mathematically by a set of coupled differential equations, known as the Navier-Stokes (NS) equations. These equations can be solved directly only at a very low Reynolds number. For the general flow, e.g., in a ventilated room, it is necessary to employ turbulence models, such as k-ε, k-ω, and v2-f models and many other models. Given the work of many researchers on benchmark experiments [29–33], numerous turbulence models have been validated for natural convection, forced convection, mixed convection and strong buoyancy flow [34–36]. Based on these validations, CFD simulations were successfully used in many investigations of indoor air environments. For instance, in some studies [37–39] CFD simulations were used to predict indoor airflow velocity and temperature. In other studies, such simulations were also used to simulate air quality-related parameters such as gaseous contaminants [40–42], volatile organic compounds [43] or particle concentrations [44]. In regard to aspects of ward simulations, Nielsen’s group performed many studies on contaminant flow in the microenvironment around people [45,46]. Gao et al. modelled the particle dispersion and deposition in indoor environments [47]. Lai et al. [48] conducted an experimental and numerical study on particle distribution in a two-zone chamber. Chen et al. [49] evaluated the Markov chain model and compared it with the traditional Eulerian and Lagrangian models in terms of performance, computing cost, and robustness. Brohus et al. [50] studied the Influence of movements on contaminant transport in an operating room. Mazumdar et al. [51] studied the impact of moving objects on contaminant concentration distributions in an inpatient ward with displacement ventilation. Cheong and Phua [52] investigated three ventilation strategies in an isolation room of a hospital. In their study, strategy 3 has the best pollutant removal efficiency. Their study can provide a constructive reference for our ventilation study on a prefabricated inpatient ward even though they have different space sizes and layouts. In a recent study, Satheesan et al. reported their numerical study of ventilation strategies for infection risk mitigation in general inpatient wards [53]. However, these studies were seldom concerned with the ventilation strategy of a prefabricated COVID-19 inpatient ward.

This study focuses on the ventilation strategy of a prefabricated COVID-19 double-patient ward. The prefabricated inpatient ward has its special characteristics, such as the fixed special size. However, there is no published study on their ventilation before this manuscript. In this manuscript, numerical simulations were implemented for three ventilation strategies in a prefabricated inpatient ward. The three ventilation strategies were used in practical settings in three prefabricated hospitals of China. Due to their use in emergency situations, the ventilation strategies may not be well designed. To understand the effect of different ventilation strategies, this manuscript provides a detailed comparison and study of the three ventilation strategies in a prefabricated COVID-19 inpatient ward.

The employed CFD method is initially verified and validated by simulations of benchmark cases. The grid sensitivity is assessed and analysed as well as the accuracy of turbulence modelling. Based on the verification and validation, numerical simulations are implemented on three ventilation strategies that have been used in practice in three prefabricated hospitals, respectively. In these simulations, both respiratory droplets and aerosols are modelled by Lagrangian multiphase analysis according to the characterizations of coughing [12]. During the post-processing, airflow velocities, air temperatures and airborne contaminant distributions are analysed and compared with each other. The predicted fate of particles is studied and analysed quantitatively.

2. Methodology

In this study, the airflow movement and the airborne transmission in the ward are investigated using an open-source CFD code (OpenFOAM v1906) [55]. The SprayFoam solver is modified and used to simulate the particle (respiratory droplets and aerosols) injection in a three-dimensional compressible turbulent non-reaction flow. (The chemistry and combustion components have been deactivated in the running simulations.) To investigate the dispersed flow of inert particles, the numerical simulation employs an Eulerian–Lagrangian model that includes a continuum phase (air) and a discrete phase (particles).

2.1. The Eulerian–Lagrangian model

In an Eulerian–Lagrangian model, the governing equations for the continuum (fluid) phase are based on an Eulerian framework, and the discrete (particle) phase is modelled by a Lagrangian framework [56]. The mass and momentum transport equations in the fluid phase can be simply described by the Reynolds-averaged Navier-Stokes (RANS) equations. In RANS equations, the Reynolds stresses are commonly modelled using an eddy-viscosity approach. According to Zhang's study and summary [36], the RNG k-ε model works well within forced convection and mixed convection cases. Hence, the RNG k-ε model is adopted in running the simulations. However, turbulence modelling will be still verified and validated by benchmark cases in the next section.

For the dispersed phase, the particle motion is solved by integrating the force balance in a Lagrangian frame. In this study, the particles (respiratory droplets and aerosols) are very small compared to the ward length and their concentration is not very high in coughs. Therefore, the particles are modelled as spherical, with no heat and mass transfer balls. According to studies by Chao [11] and Bourouiba [12], the particle (respiratory droplets and aerosols) density is 993 $\mathrm{kg/m^{-3}}$. The measured diameters of these particles range from 3 μm to 750 μm [11]. Hence, the particles can be modelled as the following equations:

$$m_p \cdot \frac{du_p}{dt} = F_D + F_B + F_G \tag{1}$$

where u_p is the particle velocity and m_p is the particle mass. The term $F_D$is the drag force, $F_B$is the buoyancy force and $F_G$is the gravitational force. The particle trajectory is controlled by these forces. The drag force implemented in SprayFoam can be described as follows:

$$F_D = \frac{3}{4}\frac{\rho}{\rho_p}\frac{m_p}{d_p} \cdot C_D\left(u-u_p\right)\left|u-u_p\right| \tag{2}$$

where d_p is the particle diameter and $C_D$is the drag coefficient. According to Crowe's book [57], the drag coefficient $C_D$is a function of the particle's Reynolds number Re_p and is calculated as given below:

$$C_D = \begin{cases} \dfrac{24}{Re_p}\left(1+\dfrac{\frac{1}{6}Re_p^2}{3}\right); & Re_p < 1000 \\ 0.424 & ; Re_p \geq 1000 \end{cases} \tag{3}$$

The buoyancy and gravitational force are calculated as follows:

$$F_B + F_G = \frac{\left(\rho_p-\rho\right)\pi d_p^3}{6} g \tag{4}$$

where g is the gravitational acceleration and the value is 9.81 $\mathrm{m/s^{-2}}$.

2.2. Coupling scheme of dispersed and continuous phases

In particle-laden simulations, the dispersed and continuous phases should be well coupled. The coupling scheme is decided by the volume fraction of the particles according to Backhander's study [58]. According to the studies of Chao [11] and Bourouiba [12], the volume fraction of the particles is low in coughs. Therefore, in this study, the particles are considered to be moving in diluting flows. In such a case, the particle's motion is primarily influenced by the aerodynamic forces acting on the particle. The particle-particle interactions and the effect of the dispersed phase on the fluid flow are negligible. Hence, a one-way coupling scheme is sufficient to model the fluid flow's influence on the dispersed phase.

2.3. Particle dispersion

The integration of particle trajectories from Equations (1)–(4) requires information about the instantaneous fluid velocity ($u = \overline{u} + u^{'}$). However, there is only Reynolds-averaged velocity ($\overline{u}$) in the RANS equations. Therefore, the fluctuating velocity $u^{'}$ has to be estimated in order to model the turbulent dispersion of the particles by either stochastic or deterministic methods.

In SprayFoam, the stochastic eddy lifetime method is applied, which is also referred to as a discrete random walk (DRW) model. In the DRW model, the values of fluctuating velocity ($u^{'}$) are sampled by assuming that they obey a Gaussian probability distribution. Consequently,

$$u^{'} = \zeta d \sqrt{\overline{u'^2}} \tag{5}$$

where ζ is a normally distributed random number, d is a random vector to depict the spatial randomness of turbulence, and the remainder of the right-hand side is the local RMS value of the velocity fluctuations. Since the kinetic energy of turbulence is known when using the RNG k-ε model, these values of the RMS fluctuating components can be defined (assuming isotropy) as

$$\sqrt{\overline{u'^2}} = \sqrt{\overline{v'^2}} = \sqrt{\overline{w'^2}} = \sqrt{\frac{2k}{3}} \tag{6}$$

2.4. Numerical schemes

The SprayFoam is a pressure-based solver using a finite volume method to discretize the NS equation. The pressure–velocity coupling is accomplished with the SIMPLE algorithm [55]. A bounded second order upwind scheme is used for the advection terms. Discretized equations are solved with the geometric algebraic multigrid (GAMG) method in conjunction with the Gauss–Seidel solver.

3. Numerical verification and validation

3.1. Verification and validation of the flow field in ventilation cases

Three benchmark experimental cases from Wang and Chen were

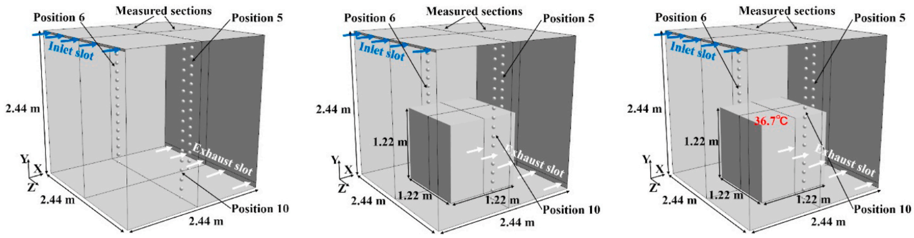

(a) Case 1: isothermal forced convection in the empty room

(b) Case 2: isothermal forced convection in the room with the box

(c) Case 3: mixed convection in the model room with the heated box

Fig. 1. Three benchmark experimental cases (reproduced from Wang and Chen [33]). The blue arrows represent the inlet flow and the white arrows represent the exhaust flow. In Wang and Chen's experiment, they measured ten probe lines (positions) on two sections. In this figure, three probe lines are shown at positions 5, 6 and 10. (For interpretation of the references to colour in this figure legend, the reader is referred to the Web version of this article.)

Table 1
Grid information and wall treatments used in benchmark cases. Compared to the grids in Wang and Chen's article [33], the coarse grid in our simulations is finer than the finest grid in their study. The fine grid in our simulations has a grid resolution close to 0.01 m in the main flow domain.

Case	Grid level	Grid resolution (cells)	Max. y^+	Wall treatment
Case 1	Coarse	128 × 150 × 128	1.50	Resolved
	Moderate	160 × 196 × 160	1.25	Resolved
	Fine	200 × 244 × 200	1.00	Resolved
Case 2	Fine	200 × 244 × 200	1.00	Resolved
Case 3	Fine	200 × 244 × 200	1.00	Resolved

chosen for verification and validation [33]. Case 1 is an isothermal forced convection case in an empty room, as shown in Fig. 1(a). The room is a square room with dimensions of 2.44 m × 2.44 m × 2.44 m. Case 2 is an isothermal forced convection in a room with a box. The only difference between Case 2 and Case 1 is the box. The box is a square box representing the furniture with dimensions of 1.22 m × 1.22 m × 1.22 m. Case 3 is a mixed convection example in the model room with a heated box. The only difference between Case 3 and Case 2 is presence or absence of a heat source. Case 3 has a heat source of 700 W. As stated by Wang and Chen [33], the heat source can heat the box surface temperature to a uniform value (36.7 °C). In all three cases, there is a linear (slot) diffuser that is located near the left wall near the ceiling. The linear diffuser has an opening height of 0.03 m along the whole width of the room and can supply a constant volume inlet flow at 0.10 m^3s^{-1} (blue arrows in Fig. 1). In the simulations, this constant volume inlet is recalculated as a velocity inlet of 1.366 ms^{-1}. The supply-air temperature is controlled at 22.2 °C. There is an exhaust slot located near the floor on the right wall. The exhaust slot has a height of 0.08 m. In the simulations, the exhaust slot is set as the pressure outlet at one standard atmospheric pressure (1 atm). As stated by Wang and Chen [33], the model room is built using insulation materials. Hence, the wall boundaries with the exception of the heated box are approximated to adiabatic walls in the simulations.

Five grids are employed in the numerical simulations of benchmark Cases 1, 2 and 3, which are listed in Table 1. These grids are high-quality hexahedra grids generated by the blockMesh in OpenFOAM. The grid topologies are shown in Fig. 2. As seen, the grids are non-uniform and have the boundary layers near the walls. The coarse, moderate and fine grids in Case 1 have the same grid topology, as shown in Fig. 2(a). Their differences are cell numbers and y + values. In the coarse grid, there are 128 × 150 × 128 cells and the max. y+ is 1.50. In the moderate grid, there are 160 × 196 × 160 cells and the max. y+ is 1.25. In the fine mesh, there are 200 × 244 × 200 cells and the max. y+ is 1.00. As can be found, the grids are well designed with an increasing rate (~1.25) in cells in each direction from the coarse grid to the fine grid. In Cases 2 and 3, the grids are the same, as shown in Fig. 2(b). There are 200 × 244 × 200 cells and the max. y+ is 1.00 corresponding to the fine grid level in Case 1. The difference is that there is a box in Cases 2 and 3. Their grid topology has a large change due to the boundary layers near the box walls. Compared to the grids in Wang and Chen's article [33], the coarse grid in our simulations is finer than the finest grid in their study. The fine grid in our simulations has a grid resolution close to 0.01 m in the main flow domain.

In Wang and Chen's work, they measured ten probe lines (positions)

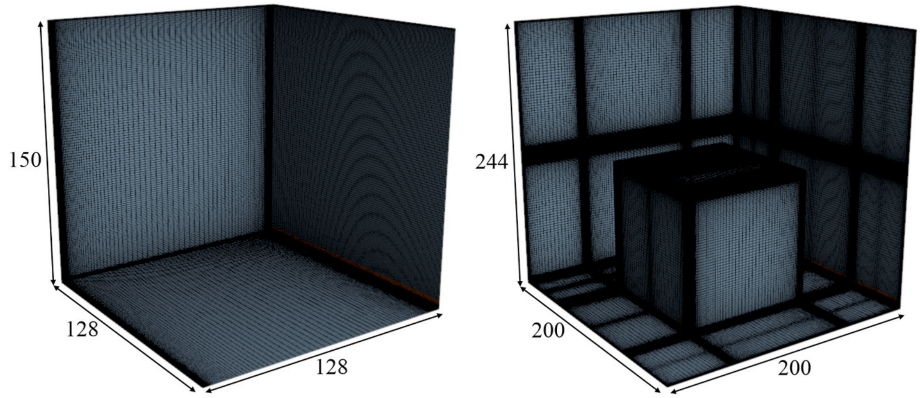

(a) Coarse grid of Case 1 (128×150×128 cells)

(b) Grids of Cases 2 and 3 (200×244×200 cells)

Fig. 2. Grid topologies used in benchmark cases. The coarse, moderate and fine grids in Case 1 have the same grid topology. Therefore, only the coarse grid is shown in (a). In Cases 2 and 3, the grids are the same as shown in (b).

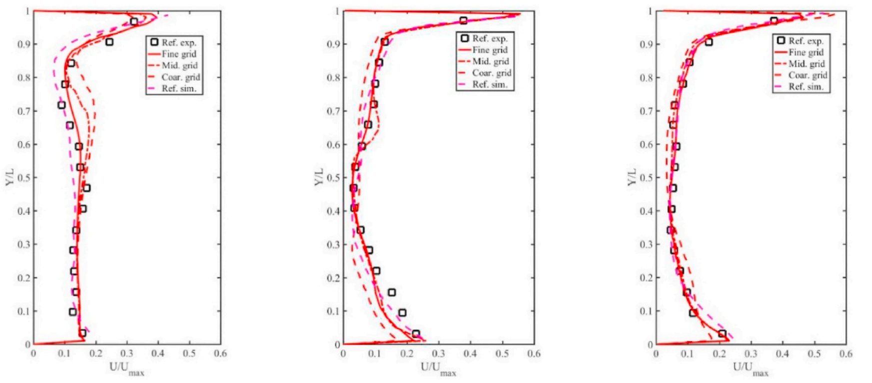

(a) Velocity profile at position 5 (b) Velocity profile at position 6 (c) Velocity profile at position 10

Fig. 3. Velocity profiles at different positions in Case 1 (Black squares denote the reference experimental data [33]. Red solid lines denote the simulation results using the fine grid. Red dot dash lines denote the simulation results using the moderate grid. Red dash lines denote the simulation results using the coarse grid. Magenta dash lines denote the simulation results using the same RNG *k-ε* model in reference article [33]). (a) Velocity profiles at position 5 that had the worst prediction in reference article [33]. (b) Velocity profiles at position 6 that had an average prediction in reference article [33]. (c) Velocity profiles at position 10 that had the best prediction in reference article [33]. (For interpretation of the references to colour in this figure legend, the reader is referred to the Web version of this article.)

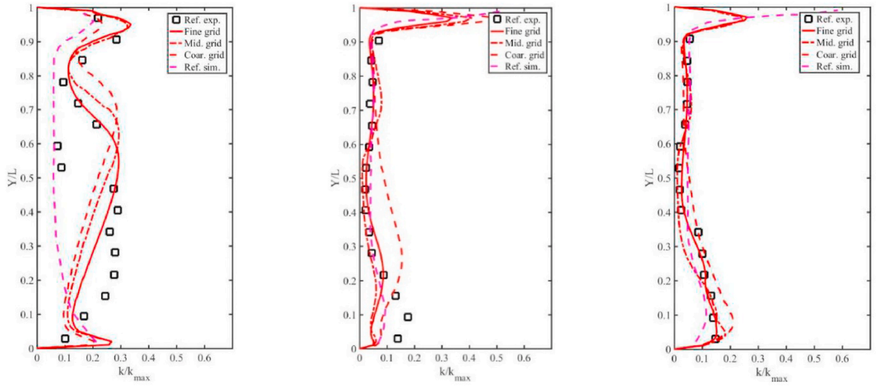

(a) Turbulence kinetic energy profile at position 5 (b) Turbulence kinetic energy profile at position 6 (c) Turbulence kinetic energy profile at position 10

Fig. 4. Turbulence kinetic energy profiles at different positions in Case 1 (the legend is the same as Fig. 3). (a) Turbulence kinetic energy profiles at position 5 (the worst positon [33]). (b) Turbulence kinetic energy profiles at position 6 (the average prediction [33]). (c) Turbulence kinetic energy profiles at position 10 (the best prediction [33]).

on two sections (see Fig. 1). One section was the cross-plane perpendicular to the inlet and exhaust slots (z-axis). The other section was the cross-section perpendicular to the x-axis. In their article, velocity and turbulence kinetic energy profiles were given in detail at positions 5, 6 and 10. Simulation results using eight different turbulence models were compared to the experimental data. At position 5, the simulation results had the worst prediction of the experimental data in their article. At position 6, the simulation results achieved an average prediction of the experimental data in their article. At position 10, the simulation results achieved the best prediction of their experimental data in their article.

To verify the grid sensitivity in our simulations, their experimental data and simulation results using the RNG k-ε model are used in the comparison with our simulation results (see Fig. 3 and Fig. 4). In Fig. 3, velocity profiles at different positions are compared among different

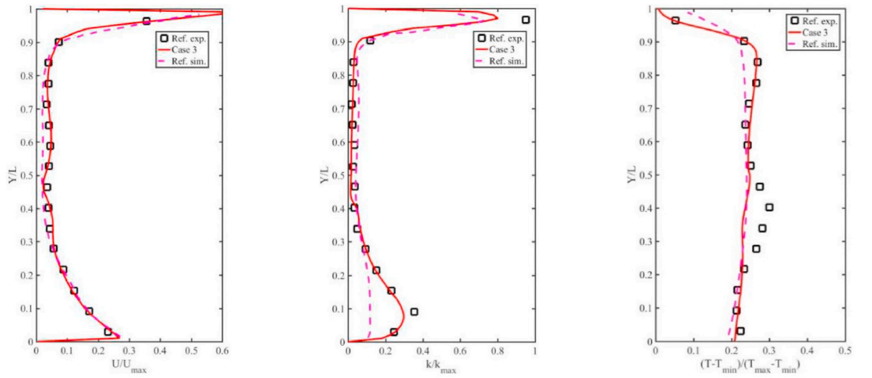

(a) Velocity profile at position 6 (b) Turbulence kinetic energy profile at position 6 (c) Temperature profile at position 6

Fig. 5. Velocity, turbulence kinetic energy and temperature profiles at position 6 in Case 3. (Black squares denote the reference experimental data [33]. Red solid lines denote our simulation results. Magenta dash lines denote the simulation results using the same RNG *k-ε* model in reference article [33].) (a) Velocity profiles at position 6. (b) Turbulence kinetic energy profiles at position 6. (c) Temperature profile at position 6. (For interpretation of the references to colour in this figure legend, the reader is referred to the Web version of this article.)

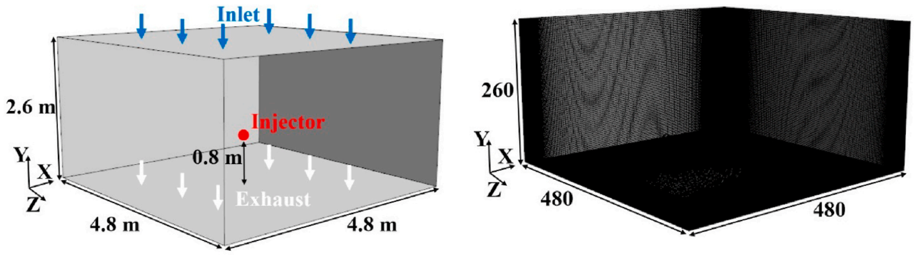

(a) Geometry of unidirectional downward flow case

(b) Grid of unidirectional downward flow case

Fig. 6. The geometry and grid of the unidirectional downward flow case. The geometry is a room with dimensions of 4.8 m × 4.8 m × 2.6 m. The blue arrows represent the inlet, and the white arrows represent the exhaust. The red point represents the injector position. The grid contains 480 × 480 × 260 cells. (For interpretation of the references to colour in this figure legend, the reader is referred to the Web version of this article.)

grids from coarse to fine. At position 5, the velocity profiles show a convergence of the experimental data. The simulation using the fine grid has the best prediction of the experimental data. At position 6, the velocity profiles show convergences with the experimental data in most of the measured points. The simulation results using the fine grid match the experimental data quite well in most of the measured points. At position 10, the velocity profiles show the best convergences to the experimental data. The velocity profiles predicted by the moderate grid almost coincide with the fine grid. They both show accurate predictions of the experimental data. In Fig. 4, turbulence kinetic energy profiles are compared with each other at different positions. At position 5, the turbulence kinetic energy profiles show a convergence from the coarse grid to the fine grid. However, they show a large deviation from the experimental data at many measured points. Position 5 is a place where the inlet flow reaches the opposite wall and moves down to the floor. The flow has a strong curvature and separations. It is difficult to accurately simulate this scenario employing RANS models. A large discrepancy can also be found between the simulation results and the experimental data in Wang and Chen's work [33]. At position 6, the kinetic energy profiles show a convergence to the experimental data. The coarse grid has a large deviation from the experimental data. Both the moderate and fine grids have good predictions with the experimental data at most of the measured points. At position 10, the kinetic energy profiles show the best convergence to the experimental data using different grids. The fine grid can produce accurate predictions of the experimental data at position 10. In general, compared to the experimental data, the simulation using the fine grid can give good predictions on velocity and turbulence kinetic energy profiles at typical positions. Compared to the reference simulation results using the same RNG k-ε model, our simulation results can achieve results that are as good as other researchers' work.

As introduced by Wang and Chen [33], the heated box in Case 3 is equivalent to the reasonable amount of heat generated by 10.5 passengers. Case 3 was designed to study the influence of thermal buoyancy flow in a room with a forced convection. It is same as the flow pattern in a ward. Therefore, Case 3 would be more appropriate than the Case 1 for the validation of our study. In Fig. 5, velocity, turbulence kinetic energy and temperature profiles in our simulation are compared to the experimental data and the reference simulation results at position 6 in Case 3. The velocity profiles in our simulation are as good as the reference simulation. Both the simulation results agree well with the measured velocity profiles. In most of the measured points, the turbulence kinetic energy profiles in our simulation show good predictions of the experimental data. Neither our simulation nor the reference simulation agrees well in some points on the top near ceiling or on the bottom near the floor. In the predictions of temperatures, our simulation and the reference simulation can give reasonable results compared to the experimental data. In some points, there is a discrepancy between the simulation results and the experimental data. In general, the velocity distribution in such a mixed convection case can be accurately simulated using the RNG k-ε model under the present grid resolution. The temperature field can be reasonably predicted. These results can give sufficient support to numerical simulations in a ward that is also a mixed convection case.

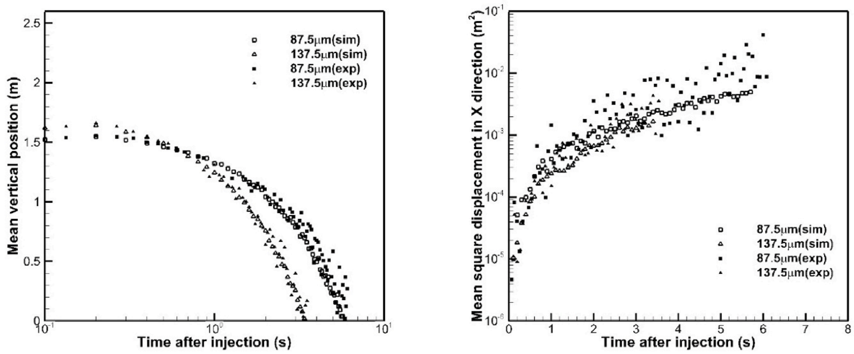

(a) Mean vertical position of droplets in the unidirectional downward flow case

(b) Mean square displacement of droplets (xz-direction) in the unidirectional downward flow case

Fig. 7. Comparison of droplet positions between simulation results and experimental data. The solid icons are experimental data, and the hollow icons are simulation results. The square icons are position data of 87.5 μm droplets. The delta icons are position data of 137.5 μm droplets.

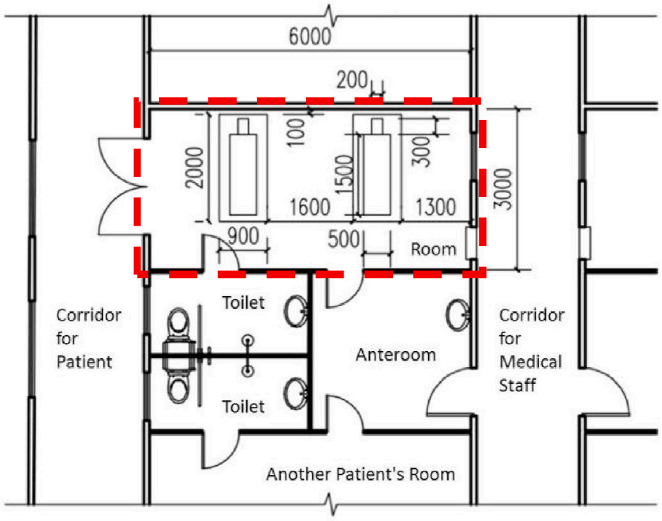

Fig. 8. A typical layout of the prefabricated ward area (the unit is mm). The two cubic rooms are a treatment cell. One cubic room is used as the inpatient ward. The other one is used for the inpatient lavatory and the clean anteroom. The two cubic rooms are isolated with sealed doors. They can be studied separately.

3.2. Validation of droplet movement

The unidirectional downward flow case in Chao and Wan's work [54] is chosen for the validation of droplet movement. The computational geometry and grid are shown in Fig. 6. The geometry is a room with dimensions of 4.8 m × 4.8 m × 2.6 m. The grid contains 480 × 480 × 260 cells (see Fig. 6(b)), a total 59,904,000 cells. The grid size in the main flow domain is approximately 1 mm. The grids close to the wall are refined to control the max. y + so that it is under 1. The unidirectional downward flow moves through the room from the ceiling to the floor, as shown in Fig. 6(a). The supply-air velocity is 0.1 m/s. The supply-air temperature is 294 K. The aerosol injection point is located at the centre of the room, 0.8 m above the floor. Aerosols (water) are injected at 10 m/s in the vertical upward direction. The injection is maintained for 1 s. Compressed air is used as the gas supply. The air flow rate is 0.4 l/s. The simulation is calculated for 10 s with a time step of 0.001 s. The detailed setup of the experiment can be found in Chao and Wan's article [54].

In this validation, droplets of 87.5 μm and 137.5 μm are adopted as injection particles. Fig. 7 shows the comparison of droplet positions between the simulation results and experimental data. The solid icons are experimental data, and the hollow icons are simulation results. The square icons are position data of 87.5 μm droplets. The delta icons are position data of 137.5 μm droplets. The mean vertical position of droplets is shown in Fig. 7(a). Due to the mirror symmetry of the geometry, the displacements in x- and z-directions are considered together in the unidirectional downward flow pattern. The mean square displacement data in the x(z)-direction is shown in Fig. 7(b). Both (a) and (b) in Fig. 7 show that the simulation and experimental results have reasonable agreement.

4. Numerical simulations of ventilation strategies for prefabricated COVID-19 inpatient ward

4.1. Case descriptions

Prefabricated wards are usually modular units of containerized cubic rooms with united form and size. These rooms can be assembled together to build a health care facility in a few days. A typical layout of a prefabricated ward area is shown in Fig. 8. Two cubic rooms are a treatment cell. One of the cubic rooms is used as the inpatient ward. Half of the room of the other one is used for the inpatient lavatory. Half of the room of the other cubic room is designed as the clean anteroom. Although these two cubic rooms are a treatment cell, they are isolated with the sealed doors. Hence, they can be studied separately. In this study, the cubic room has the dimensions of 3 m × 2.6 m × 6 m. Three ventilation strategies are employed for the comparison in this study. They are shown in Fig. 9. In ventilation strategy I, both the inlet and outlet are on the same sidewall (x-y plane at $z = 0.0$ m). They have the same square area (0.4 m × 0.4 m). The centre of the inlet is at (0.3 m, 2.3 m, 0 m) and the centre of the outlet is at (2.7 m, 0.3 m, 0 m) m. In a COVID-19 impatient ward, both the inlet and the outlet have filtration systems. The filtration systems are changed at regular intervals. Hence, the inlet and the outlet are modelled with the actual thicknesses in our simulations. The inlet has a thickness of 0.05 m and the outlet thickness is 0.2 m. In ventilation strategy II, the inlet and the outlet are on the opposite sidewalls. The inlet is on the x-y plane with a centre of (0.3 m, 2.3 m, 6.0 m). The outlet is at the same position as in ventilation strategy I. In ventilation strategy III, the inlet is on the ceiling and two outlets are installed on the sidewall opposite of the entrance door. The inlet is on the x-z plane with the centre at (0.3 m, 2.6 m, 3.0 m). There are two outlets in ventilation strategy III. They are both on the y-z plane at $x = 3$ m. The centre of one outlet is at (3 m, 0.3 m, 0.7 m). The centre of the other outlet is at (3 m, 0.3 m, 5.3 m). There are two patient models lying on two beds. The patient is modelled as two human-like cube blocks. The body from the feet to the shoulders is modelled as one block with dimensions 1.5 m × 0.5 m × 0.3 m. The head and neck are modelled as a block with dimensions of 0.3 m × 0.2 m × 0.3 m. The bed is modelled as one block with dimensions of 2.0 m × 0.9 m × 0.12 m. The lower surface has a distance of 0.4 m to the floor. The two beds have a gap of 0.1 m to the wall in the head direction. The heads of the two patients have a distance of 0.2 m to the wall. As shown in the layout (Fig. 8), the two beds have a distance of 0.9 m to the sidewall, separately. The distance between the two beds is 1.6 m.

In a typical COVID-19 inpatient ward, the flow is pumped out from the outlet(s). Hence, a negative velocity is set for the outlet. Due to the existence of the thick filtration(s) in the outlet(s), the negative velocity can have a uniform distribution on the filtration(s) surface. In ventilation strategies I and II, the velocity value is -1 ms^{-1} (in the z-coordinates) for the outlet that corresponds to an air change rate at 12.3 h^{-1}. This air change rate satisfies the requirement (>12 h^{-1}) of COVID-19 inpatient wards [19]. In ventilation strategy III, the velocity values

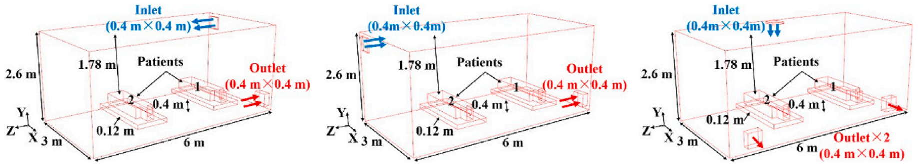

(a) Ventilation strategy I (b) Ventilation strategy II (c) Ventilation strategy III

Fig. 9. Ventilation strategies for a prefabricated isolation ward. (a) Ventilation strategy I: both the inlet and outlet are on the same sidewall; (b) Ventilation strategy II: the inlet and the outlet are on the opposite sidewalls; (c) Ventilation strategy III: the inlet is on the ceiling and two outlets are installed on the wall opposite the entrance door.

Table 2
Particle samples in this study. (The six samples come from the coughing measurement in Refs. [11,12]).

Size range (μm)	2–4	4–8	8–16	16–24	40–50	150–200
Modelled size (μm)	3	6	12	20	45	175
Particle numbers	76	1041	386	127	38	83

are 0.5 m/s (in the x-coordinates) for each outlet. The air change rate remains the same as ventilation strategy I and II. The inlet boundary conditions in all three ventilation strategies are set as the pressure outlet. The walls of the cubic room are filled with insulation materials. Hence, these walls are approximated as adiabatic walls. The bases of the inlet and outlet are covered by plastic materials and approximated as adiabatic walls. The beds are covered by mattresses and bedclothes. They are considered adiabatic walls. The two patients are represented as isothermal walls with a temperature at 36.7 °C.

In this study, both respiratory droplets and aerosols are modelled as injected particles with different diameters. On the basis of experimental observations on coughing [11,12], a cone injector model is used to make sure that coughing flow is simulated correctly. In Chao's [11] experiments, the average expiration air velocity was 11.7 m/s for coughing. In Bourouiba's [12] study, the average coughing velocity was measured to be 11.2 m/s. The COVID-19 inpatients often have incessant violent coughing. A single cough is a pulse flow injected from the patient's mouth. However, the incessant coughing process is normally disorderly, different from time to time. There are two patients in a prefabricated COVID-19 inpatient ward. The individual differences between the coughing processes are normally unclear between the two patients. To get a general consideration for the ventilation study, the coughing process is simplified as a continuous inlet flow with the measured velocity of 11.7 m/s. The simulation started with a steady RANS simulation. When it reaches a quasi-steady result, the simulation was changed to a transient simulation for 1000 s. The time step is 0.001 s. In Chao's [11] study, they measured the droplet size distributions from 2 to 2000 μm. In this study, six particle samples are selected for simulation, as

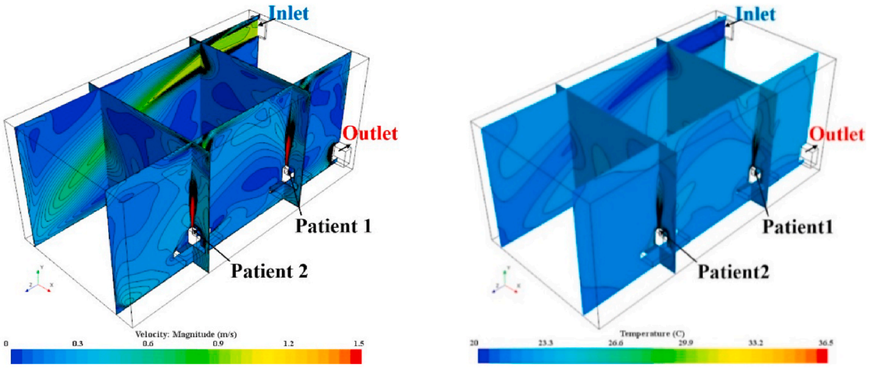

(a)Velocity distribution in ventilation strategy I (b) Temperature distribution in ventilation strategy I

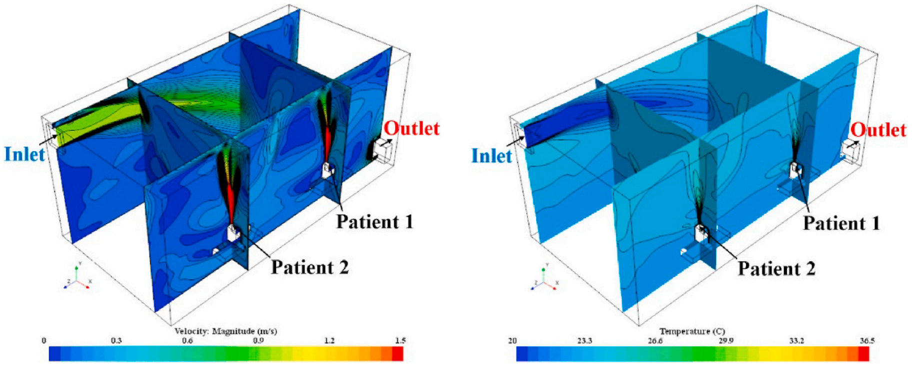

(c) Velocity distribution in ventilation strategy II (d) Temperature distribution in ventilation strategy II

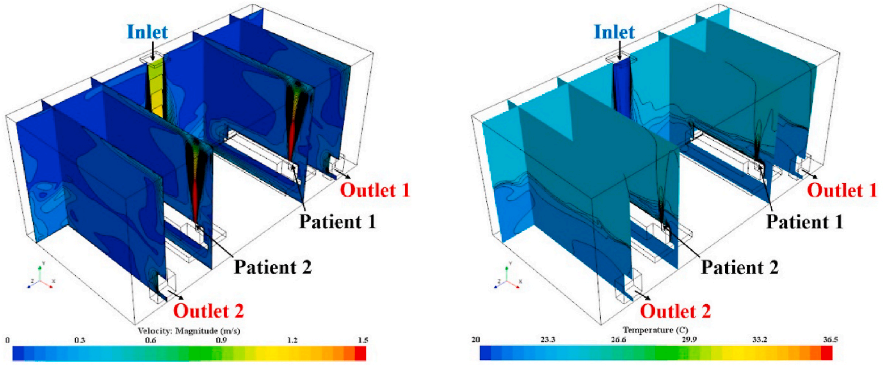

(e) Velocity distribution in ventilation strategy III (f) Temperature distribution in ventilation strategy III

Fig. 10. Overall comparison of flow fields among three ventilation strategies. (a), (c) and (e) are velocity distributions on several cross-planes in the three ventilation strategies. (b), (d) and (f) are temperature distributions on the same cross-planes in the three ventilation strategies.

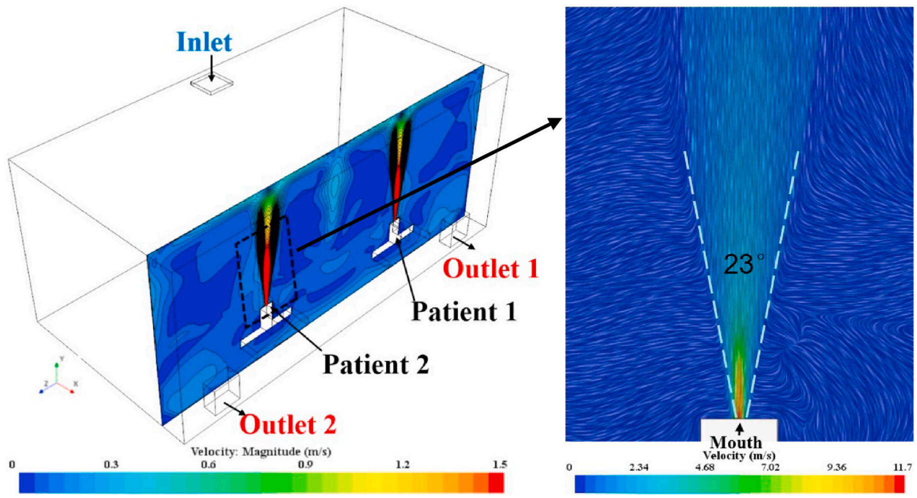

Fig. 11. Validation of coughing flow (injected from the mouth of patient 2 in ventilation strategy III). The left figure shows the flow fields of velocity magnitude on the cross-section of patients' mouths in ventilation strategy III. The right figure shows the line integral convolution of injected flow (dashed area in the left figure) Please note the change of legends in the two figures. The coughing flow has an initial speed of 11.7 m/s. The coughing flow is a cone that has an opening angle of 23° which agrees well with the observation in experiments (23.9 ± 3.4°) [11,12].

shown in Table 2. The values of "size range", "modelled size" and "particle numbers" are completely from the Chao article [11]. The particles' diameters of the first sample range from 2 to 4 μm. The modelled size is 3 μm. This is the typical size of aerosols. The particles' diameters of the second sample range from 4 to 8 μm. The modelled size is 6 μm. This size is the critical value from aerosols to respiratory droplets. The particles' diameters of the other 4 samples are larger than 10 μm. They are considered respiratory droplets with different sizes. The cone injector models are in the +y-direction and positioned on the mouth of the two inpatients. The position of one patient's mouth is at (1.75, 2.7, 0.82) m. The position of the other patient's mouth is at (1.25, 2.7, 0.82) m. The mouth opening area is set as 4 cm^2 during the cough, which is also consistent with values reported in previous studies: 4 ± 0.95 cm^2 for males and 3.37 ± 1.4 cm^2 for females [60].

The grids employed in the three ventilation strategy cases are made using the same method (snappyHexMesh and blockMesh) in OpenFOAM. They have the same grid size in the flow domain. The grid resolution is 0.01 m. This size is finer than the fine grid used in the validation cases. Near the wall boundary, 4 boundary layers are added with an expansion ratio of 1.1. The maximum y+ is controlled to be under 1.0. The total number of cells is approximately 50 million in each grid. The employed turbulence model and the numerical schemes in ventilation strategy cases are the same as the validation cases.

4.2. *Results and discussion*

4.2.1. *Overall comparison of flow fields among three different ventilation strategies*

The overall comparison of flow fields among three different ventilation strategies is shown in Fig. 10. Fig. 10 (a), (c) and (e) are velocity distributions on several cross-planes in the three ventilation strategies. Fig. 10 (b), (d) and (f) are temperature distributions on the same cross-planes in the three ventilation strategies.

In ventilation strategy I, both the inlet and the outlet are located in the same sidewall at $z = 0$ m. The inlet locates on the upper left corner. The outlet locates on the lower right corner. The contaminated air is pumped out from the outlet with a uniform speed of 1 m/s. The fresh air is supplied from the inlet due to the negative pressure circumstance in the ward. As can be observed in Fig. 10 (a), the inlet flow is sucked into the ward and resembles a jet that is normal to the sidewall. The inlet flow is colder than the air in the ward, see Fig. 10 (b). Due to gravity, the inlet flow is bended to the ground and reaches the ground corner. Two hot jet flows are found above the faces of the two patients. They are produced by the coughing process. The coughing jet velocity can reach as high as 11 m/s. In ventilation strategy I, the coughing jet flow is not a standard cone shape but is bent to the outlet. From an overall perspective, the flow fields in ventilation strategy I are chaotic with large-scale motion inside. There are three low-velocity regions: the intersection corner between the ceiling and the sidewall at $z = 6$ m, the isolation area between the two patients and the corner under the inlet. In these low-velocity regions, the contaminated air will require a long refresh time. Respiratory droplets and aerosols may stay at these regions or fall on nearby object surfaces.

In ventilation strategy II, the inlet and the outlet are in opposite sidewalls. The inlet is located at the upper left corner on the sidewall at $z = 6$ m. The outlet on the lower right corner is the same as in ventilation strategy I. The polluted air is pumped out from the outlet with a uniform speed of 1 m/s. As can be found in Fig. 10 (c) and (d), the inlet flow is sucked into the ward and bent to the ground. This inlet flow pattern is similar to the inlet flow in ventilation strategy I. However, they have different flow directions. Above the faces of the two patients, there are also two coughing jet flows. However, there is a slight difference between the two coughing jet flows. In the same cross-planes, the coughing jet flow in ventilation strategy II has a larger high-speed area than the coughing jet flow in ventilation strategy I. The coughing jet flow in ventilation strategy II has a standard cone shape with the axis vertical to the ceiling. The integral flow field in ventilation strategy II is similar to the flow field in ventilation strategy I. It is also chaotic with large-scale motion inside. The low-velocity regions are the intersection corner between the ceiling and the sidewall at $z = 0$ m and the region between patient 2 and the sidewall at $z = 6$ m. These two low-velocity regions would be the holding area of the virus.

In ventilation strategy III, there are two outlets on the sidewall at $x = 3$ m. The contaminated air is pumped out from the two outlets with the same speed of 0.5 m/s. The inlet locates on the ceiling. As can be found in Fig. 10(e and f), the fresh air is sucked and falls straight on the ward ground. Hence, this flow pattern is quite different from the other two ventilation strategies. In ventilation strategy III, there are also two hot jet flows caused by the coughing process. These two coughing flow patterns are similar to the coughing jet flows in ventilation strategy II. The coughing jet flows are shaped as cones with the axes normal to the ceiling. The flow field in ventilation strategy III is different from the other two ventilation strategies. In ventilation strategy III, the inlet flow has less of an effect on the integral flow. There are large low-velocity regions above the patients in the ward (see Fig. 10(e)). As a result, the temperature field is divided into two regions. The temperature in the region above the patients is clearly higher than the temperature in the region below patients. The flow field above the patients is quite steady. In such a steady flow field, the respiratory droplets and aerosols would remain in suspension in the air for a long time. The contaminated air

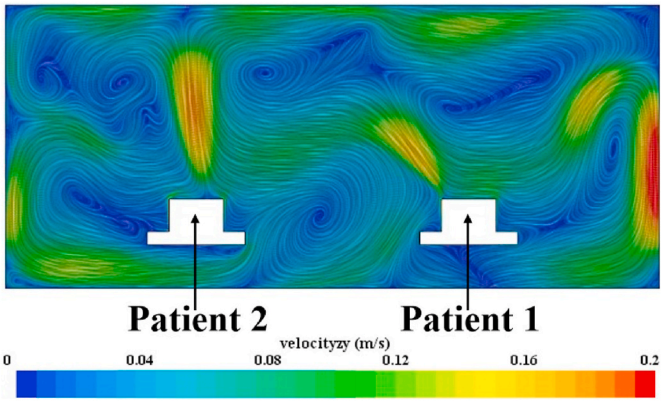

Fig. 12. Line integral convolution at mid-cross-section (x = 1.5 m) in ventilation strategy II. The body plumes can be observed around the body sections of two patients. On the top of patient 2, the body plumes can rise and form two vortexes when they are curled by the ceiling. However, such an upflow cannot be observed on the top of patient 1. The body plumes are blown away by the ventilation inlet flow.

cannot be refreshed in time.

4.2.2. *Validation of coughing flow and body plumes*

As reviewed in reference article [20], the spread of droplet nuclei between occupants of the same indoor space is strongly influenced by the complex interaction of ventilation flow, body plumes, and respiratory flow (coughing flow in this study). Though ventilation is widely recognized as the most conducive to engineering methods for controlling airborne transmission indoors [9,61,62], the body plumes and the coughing flow may also have important roles.

In this study, the characterizations of actual coughing flow [11,12] are employed. The boundary conditions of injected flow have been introduced in the case description. Fig. 11 shows the validation of coughing flow. The selected coughing flow is on the cross-section of patients' mouths (see the left figure in Fig. 11). The initial speed of coughing flow is 11.7 m/s. This illustrates that the boundary conditions are loaded correctly for particle movements in the simulations. The coughing flow is a cone. The opening angle is 23° in the right figure of Fig. 11. This value agrees well with the observations in experiments [11, 12]. In their experiments, the opening angles are 23.9 ± 3.4°. This indicates that the coughing flow is well simulated in our simulations.

The body plumes of a thermal manikin have an important influence on its microenvironment, especially when the local ventilation flow is relatively weak [20,23]. Fig. 12 shows the line integral convolution at mid-cross-section (x = 1.5 m) in ventilation strategy II. The body plumes can be observed clearly around the body sections of two patients. On the top of patient 2, the body plumes can rise and form two vortexes when they are curled by the ceiling. However, the upflow generated by the body plumes are very weak. The velocities of the upflow are less than 0.2 m/s. Compared to the coughing flow (11.7 m/s) and the ventilation inlet flow (1 m/s), the body plumes are much weaker and easily broken up. For example, the upflow cannot be observed on the top of patient 1. The body plumes are blown away by the ventilation inlet flow (shown in Fig. 12). This indicates that the body plumes are not the dominant flow in this study. This study focuses on the airborne transmission under different ventilation strategies but not the thermal comfort or the cross-infection of the two patients. Therefore, the body plumes from manikins may not be the key factors in this study.

4.2.3. *Main flow structures and particle trajectories*

In the overall comparison, the flow fields are mainly dominated by the large-scale motions in different ventilation strategies. To analyse the large-scale motions more clearly, we use the freestreams to show the flow structures in the three ventilation strategies. There are mainly three flow structures found in each ventilation strategy: the inlet-outlet flow and the two coughing jet flows above the patients. Figs. 13, 15 and 17 show the streamlines of the flow field in ventilation strategies I-III, respectively. To access the distribution of respiratory droplets and aerosols, particle trajectories are shown in Figs. 14, 16 and 18. The respiratory droplets and aerosols are modelled particles with different

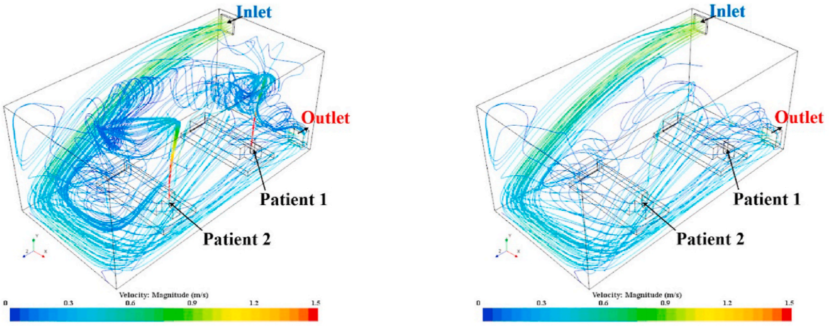

(a) Superimposed streamlines

(b) Streamlines seeded from the inlet to the outlet

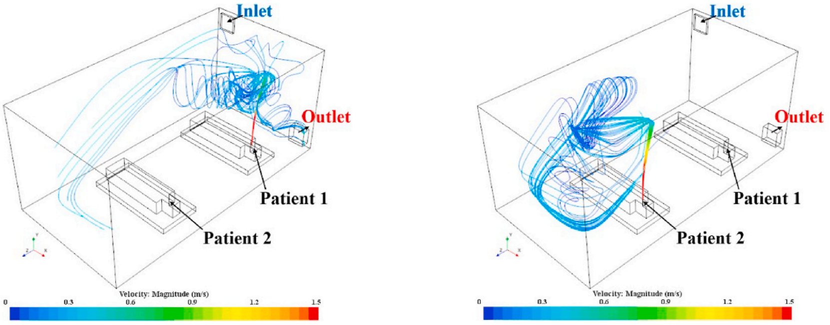

(c) Streamlines seeded from the mouth of patient 1

(d) Streamlines seeded from the mouth of patient 2

Fig. 13. Flow streamlines in ventilation strategy I. (a) is the superimposed streamlines of (b), (c) and (d). The inlet-outlet flow forms a "U" type of structure that can have a large effect on the coughing jet flows.

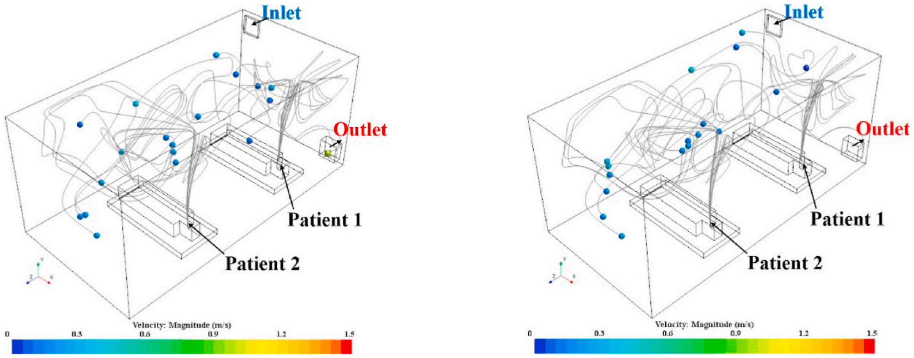

(a) Trajectories of 3 µm particles

(b) Trajectories of 6 µm particles

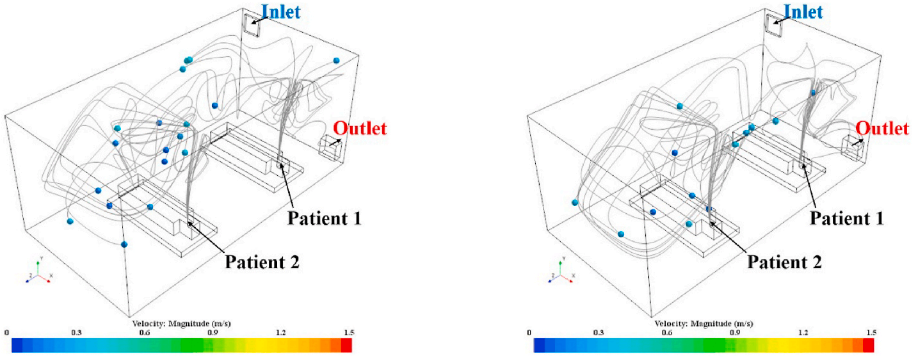

(c) Trajectories of 12 µm particles

(d) Trajectories of 20 µm particles

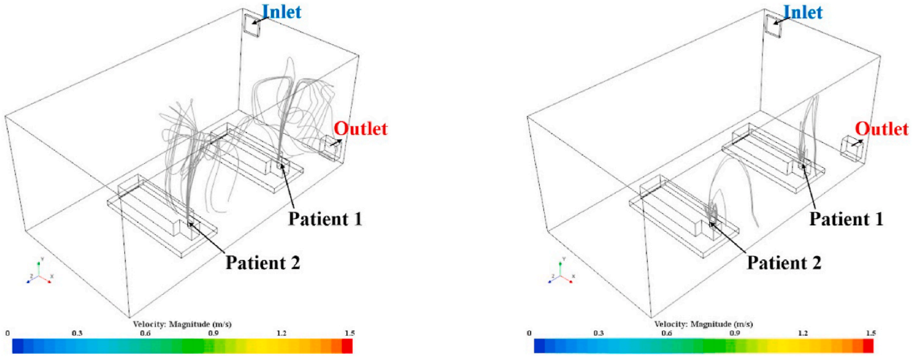

(e) Trajectories of 45 µm particles

(f) Trajectories of 175 µm particles

Fig. 14. Particle trajectories in ventilation strategy I. When particle diameters are smaller than 20 µm, the particles move along with the main flow structures. Some particles from patient 1can exit from the outlet directly. When particle diameters are larger than 45 µm, the particles fall onto the solid surfaces near the patients' head, the corridor between the two patients and the region near the outlet.

diameters from 3 µm to 175 µm. The details are listed in Table 2. In each coughing jet flow, there are thousands of particles. However, in the post-processing, we only show 10 particles for each diameter in each coughing jet flow. For example, in Fig. 14(a), the coloured balls denote the particles and the grey curves denote the trajectory of each particle. When the particles fall on any solid surface, they will disappear but their trajectories will be retained, for example, in Fig. 14(e).

In ventilation strategy I, the main flow structures can be assessed in Fig. 13. Fig. 13 (a) is the superimposed streamlines of the three main flow structures, which can give an overall view of the three flow structures. To show the main flow structures more clearly, Fig. 13 (b) gives the streamlines seeded from the inlet to the outlet, Fig. 13 (c) gives the streamlines seeded from the mouth of patient 1, and Fig. 13 (d) gives the streamlines seeded from the mouth of patient 2. As can be found in Fig. 13 (b), the inlet flow is sucked into the ward and forms a jet-like flow. The velocity is approximately 1 m/s. It bends to the ground until it reaches the corner at (0, 0, 6) m. When the inlet flows reach the corner, most of them are curled in the x-direction along the sidewall at z = 6 m. A small part of the inlet flow is curled along the y-direction and forms a circulation flow at the corner (0, 2.6, 6) m. The mainstream of the inlet flow goes along the sidewall (z = 6 m) and is curled again at the corner (3, 0, 6) m. After this turn on the corner, the mainstream of the inlet flow diffuses around the patients with a decreasing speed. Finally, the mainstream exits from the outlet. The flow structure forms a "U" type of shape from the inlet to the outlet. In Fig. 13 (c) and (d), the coughing jet flows have very high initial speed up to 11 m/s. This speed is unexpected. However, it comes from the experimental data [11,12]. With this high initial speed, the coughing jet flows can reach the ceiling. Then, they are curled and diffused to the surroundings. Compared to the coughing jet flows in Fig. 15 (c) and (d) in ventilation strategy II, these two coughing jet flows in ventilation strategy I incline slightly to the outlet. This is due to the main stream of the inlet flow. As seen in Fig. 13 (c), the coughing jet flow from patient 1 diffuses similar to a cloud near the ceiling. The speed of this coughing jet flow decreases nearly to zero. Some of the coughing cloud is involved in the inlet flow. Some of the coughing cloud goes to the outlet. As seen in Fig. 13 (d), the coughing

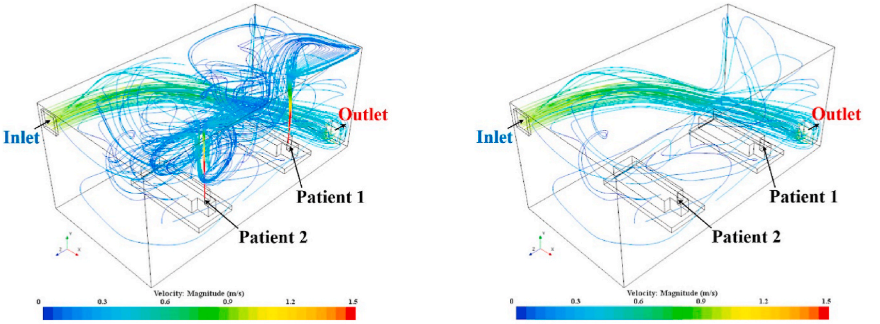

(a) Superimposed streamlines (b) Streamlines seeded from the inlet to the outlet

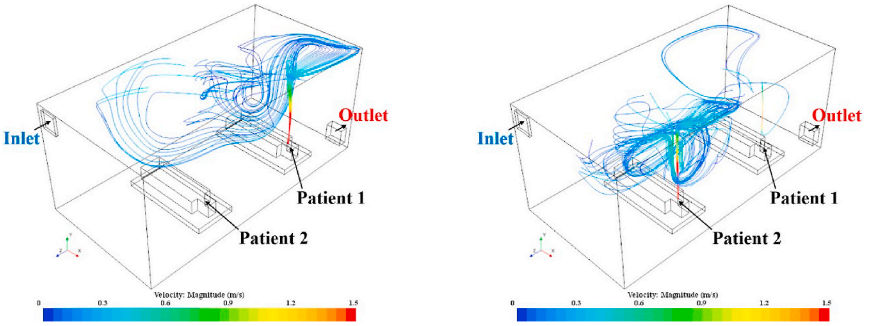

(c) Streamlines seeded from the mouth of patient 1 (d) Streamlines seeded from the mouth of patient 2

Fig. 15. Flow streamlines in ventilation strategy II. (a) is the superimposed streamlines of (b), (c) and (d). The inlet-outlet flow in ventilation strategy II forms an “L” type of structure that has less of an effect on the coughing jet flow than that of the ventilation strategy 1.

cloud from patient 2 is also involved in the inlet flow as a “U” type of structure.

Particle trajectories in ventilation strategy I are shown in Fig. 14. In Fig. 14(a), the particle diameter is 3 μm. There are 19 coloured balls, which is less than the injected 20 particles. Hence, one particle has fallen on a solid surface. Observing the particle trajectories one by one, we can find this particle has fallen on the outlet and disappeared. As seen in Fig. 14 (a), these particles move along with the main flow structures. When they are sprayed in the mouths of the two patients, they follow the coughing jet flow and will be curled near the ceiling. When they move inside the coughing cloud, they will be involved in the main stream of the inlet-outlet flow. In Fig. 14 (b), the particle diameter is 6 μm. The particle trajectories in Fig. 14 (b) are similar to Fig. 14 (a). However, there are 17 coloured balls shown in Fig. 14 (b), which means three particles have fallen on a solid surface and disappeared. In Fig. 14 (c) and (d), the particle diameters are 12 μm and 20 μm, respectively. Their particle trajectories look similar to each other. The particle trajectories form a “U” type of shape following the main stream of the inlet-outlet flow. However, there are only 14 coloured balls in Fig. 14 (d), which is much less than that in Fig. 14 (a), (b) and (c). In Fig. 14 (e) and (f), the particle diameters are 45 μm and 175 μm, respectively. There are no coloured balls found in Fig. 14 (e) and (f). The particles are too large to move with the main flow structures. Due to gravity, the particles have fallen down. In Fig. 14 (e), the particles have fallen down on two zones. One zone is the region between patient 1 and the sidewall at z = 0 m. The other zone is the region between the two patients. In Fig. 14 (f), the particles have fallen onto the nearby surface around the patients’ head. In summary, when particle diameters are smaller than 20 μm, the particles move along with the main flow structures. When particle diameters are larger than 45 μm, the particles fall onto the surrounding solid surfaces. The regions near the patients’ heads, the corridor between the two patients and the region near the outlet are the main polluted surfaces in ventilation strategy I.

In ventilation strategy II, the main flow structures can be seen in Fig. 15. Fig. 15(a) shows the superimposed streamlines of the three main flow structures. Fig. 15(b) gives the streamlines seeded from the inlet to the outlet. Fig. 15(c) gives the streamlines seeded from the mouth of patient 1. Fig. 15 (d) gives the streamlines seeded from the mouth of patient 2. Compared to the inlet-outlet flow in ventilation strategy I, the inlet-outlet flow in ventilation strategy II has similar characteristics. The inlet is on the sidewall at z = 6 m. Due to the negative pressure, the inlet flow is sucked into the ward and forms a jet-like flow in the negative z-direction. Similar to the inlet flow in ventilation strategy I, the inlet flow in ventilation strategy II bends to the ground and curls at the corner. Different from the inlet flow in ventilation strategy I, the inlet flow in this ventilation strategy is only curled at one corner at (0, 0, 0) m. Then, the inlet flow moves along the sidewall at z = 0 m and exits the ward by the outlet. Hence, the inlet-outlet flow forms an “L” type of shape. The coughing jet flow of patient 1 is shown Fig. 15(c). The coughing jet flow of patient 1 sprays vertically to the ceiling. When it approaches the ceiling, it is curled to the corner (3, 2.6, 0) m. Then, it is rotated again by the corner and moves to the opposite direction to the top of patient 2. Finally, the coughing jet flow of patient 1 is involved in the inlet-outlet flow. The coughing jet flow from patient 2 sprays vertically to the ceiling and forms a coughing cloud. Some of the coughing cloud diffuses to the top of patient 1. The other coughing cloud is involved in the inlet-outlet flow.

Particle trajectories in ventilation strategy II are shown in Fig. 16. As seen in Fig. 16 (a)–(d), the trajectories look similar among 3 μm, 6 μm, 12 μm and 20 μm particles. These particles move along the main flow structures. When these particles are sprayed from the mouths of two patients, they follow the two coughing jet flows. When the coughing jet flows are curled, these particle trajectories show similar curls to the main stream lines. The particles from the mouth of patient 1 do not exit from the outlet directly. However, they move to the top of patient 2. The particles from the two patients show an interaction at the top of the two patients. Finally, some particles are involved in the main stream lines of the inlet-outlet flow. In Fig. 16 (e), the particle diameter is 45 μm. These particles are too large to move along the main flow structures for a long way. None of the coloured balls are found in the ward. The particles have fallen on the region between the patient 2 and the sidewall z = 6 m. In Fig. 16 (f), the particle diameter is 175 μm. The particles are sprayed for

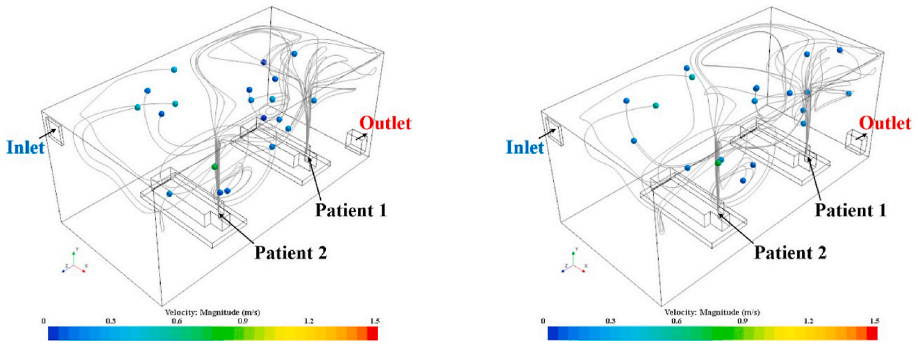

(a) Trajectories of 3 μm particles (b) Trajectories of 6 μm particles

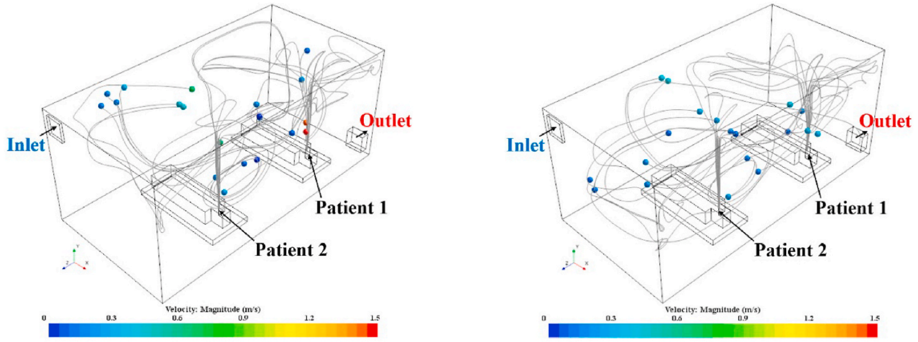

(c) Trajectories of 12 μm particles (d) Trajectories of 20 μm particles

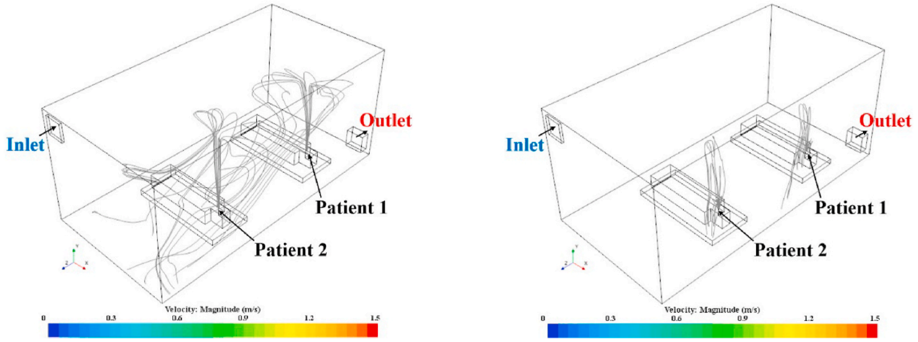

(e) Trajectories of 45 μm particles (f) Trajectories of 175 μm particles

Fig. 16. Particle trajectories in ventilation strategy II. When particle diameters are smaller than 20 μm, the particles from patient 1 do not exit from the outlet directly but move to the top of patient 2. The particles from the two patients show an interaction at the top of the two patients. When particle diameters are larger than 45 μm, the particles fall onto the solid surfaces near the patients' head, the ground between the two patients and the region between patient 2 and the sidewall z = 6 m.

a certain height. Then, they fall on the solid surface near the patients' heads. Some of them fall on the ground between the two patients.

In ventilation strategy III, the main flow structures (see Fig. 17) are quite different from the ventilation strategies I and II. As shown in Fig. 17(b), the inlet flow is sucked into the ward from the ceiling to the ground. When the inlet flow hits the ground, it scatters to the surroundings. Because the inlet flow is colder than the original air, the inlet flow diffuses on the ground and has less effect on the two coughing jet flows. The inlet flow moves under the bed and exits from the two inlets. In Fig. 17(c), the coughing jet flow of patient 1 sprays vertically to the ceiling and scatters similar to a coughing cloud. Most of the coughing cloud diffuses to the sidewall z = 0 m. A small part of the coughing cloud is involved into the inlet flow. In Fig. 17(d), the coughing jet flow of patient 2 has similar characteristics to the coughing jet flow of patient 1. Compared to the main flow structures in ventilation strategies I and II, the coughing jet flow structures are less affected by the inlet-outlet flow in ventilation strategy III.

Particle trajectories in ventilation strategy III are shown in Fig. 18. The trajectories of small (<20 μm) particles are similar to each other (Fig. 18 (a)–(d)). The small particles are sprayed from the mouths of the two patients. They can move along the main flow structures. These small particles follow the coughing jet flow to the ceiling and diffuse in all directions. Some of the particles meet the sidewalls and change their directions to the ground. Some of them change their direction back to the patients. Some of them are involved in the inlet-outlet flow. In Fig. 18 (e), the particle diameter is 45 μm, and the particles are sprayed for certain height. Then, they fall onto the solid surface and disappear. Their trajectories appear to be an umbrella. They fall onto the bed, the outlet and the ground near the patients' heads. In Fig. 18 (f), the particle diameter is 175 μm. The particles are sprayed and fall onto the bed near the patients' heads.

4.2.4. *Predicted fate of particles*

From the analysis of main flow structures and particle trajectories, we can find that smaller particles are easily influenced by airflow and can travel a long distance, while large particles tend to deposit on

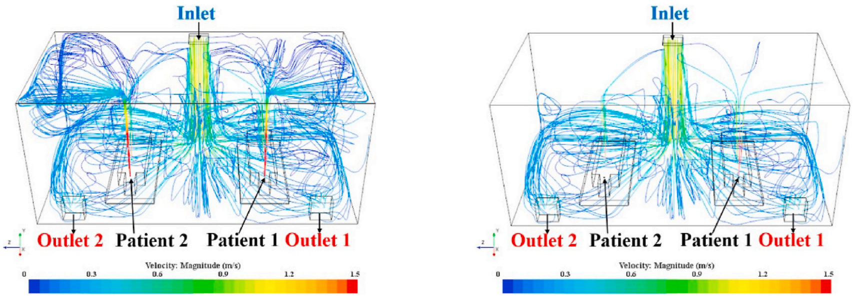

(a) Superimposed streamlines (b) Streamlines seeded from the inlet to the outlet

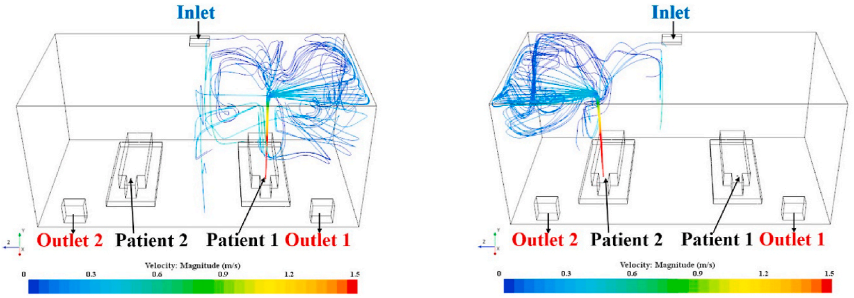

(c) Streamlines seeded from the mouth of patient 1 (d) Streamlines seeded from the mouth of patient 2

Fig. 17. Flow streamlines in ventilation strategy III. (a) is the superimposed streamlines of (b), (c) and (d). The inlet-outlet flow is from the ceiling to the ground, which has little effect on the coughing jet flows.

surfaces close to the source. Table 3 summarizes the percentage of particles (in different diameters) suspended in the air and those removed by two major mechanisms, i.e., by ventilation to the exhaust outlet(s) and by deposition on different surfaces. These are calculated by adding up the total particles (in different diameters) removed or suspended by each mechanism after the particles are released continuously for 1000 s.

Looking at the small particles (<20 μm) in Table 3, most of them are removed by the ventilation mechanism to the exhaust outlet in the three ventilation strategies. In ventilation strategy I, approximately 86.1–88.7% of the small particles are removed by ventilation to the outlet, with approximately 4.3–5.1% suspended in the air, and approximately 6.2–9.6% found on different surfaces. In ventilation strategy II, approximately 83.4–85.4% of the small particles are removed by ventilation to the outlet, with approximately 6.2–7.4% suspended in the air, and approximately 7.2–10.4% found on different particles. In ventilation strategy III, approximately 64.3–67.3% are removed by ventilation to the outlet, with approximately 18.4–26.3% suspended in the air, and approximately 6.4–17.3% found on different surfaces. From the comparison of above statistics, the number of suspended particles in ventilation strategy III are greater than the number of suspended particles in ventilation strategies I and II. Under the consideration of ventilation efficiency, the ventilation strategy I is better than ventilation strategy II. They are both much better than the ventilation strategy III. The particles on the ceiling and walls are worthy of discussion. When particles are injected from the patient's mouth, the initial velocity is 11.7 m/s. It is very fast. The particles can reach the ceiling and then diffuse in all directions. During this process, some particles can adhere to the ceiling and surrounding walls. This mechanism is quite different from ventilation and deposition mechanisms. However, the percentages of particles on the ceiling and walls are quite small compared to the two major mechanisms. Hence, it will not be discussed as key mechanisms in this study.

Looking at large particles (>45 μm) in Table 3, most of them are found on different surfaces. In all the three ventilation strategies, 60.6–71.6% of the 45 μm particles deposit on the floor, with 13.4–18.8% on the beds and 3.1–7.5% on the manikins' skin. In contrast, the particles removed by ventilation to the outlet(s) account for only 0–18.1% in the three ventilation strategies. With the analysis of particle trajectories in different ventilation strategies, the removal efficiency by ventilation for 45 μm particles is obviously affected by the distance from the particle source to the exhaust outlet(s). For 175 μm particles, approximately 5.3%–10.6% of 175 μm particles deposit on the floor, with 43.8–53.6% on the beds and 41%–45.5% on the manikins' skin. This indicates that when particle diameters are large enough, the injected particles deposit near the patients mouths. In summary, for the large particles (>45 μm), the number of particles removed by deposition are much greater than by ventilation to the outlet(s).

5. Limitations

There are four limitations in the current study. The first limitation is the modelling of respiratory droplets and aerosols. Because this research focuses on the ventilation strategies, the respiratory droplets and aerosols are not accurately simulated. The complicated vapour liquid phase change is not included in the study. The particle-particle interactions are neglected. The second limitation is the setting of coughing process. Since it is more meaningful to obtain a general consideration of ventilation study, the disorderly unsteady coughing processes of different patients are not considered in the study. The individual differences of distinct patients are not considered in the model of coughing processes. The coughing process is simplified as a continuous inlet flow. The injected flow and particle's data come from the experimental data proposed by Chao [11] and Bourouiba [12] which represents averaged results of diverse people. The manikin models used in this study are rough. This is the third limitation in this study. The body plumes are quite weaker than the coughing flow and the ventilation flow (Fig. 12). This study focuses on the airborne transmission under different ventilation strategies but not the thermal comfort or the cross-infection of the two patients. Hence, the manikin models are simplified without unnecessary details. The prefabricated COVID-19 inpatient ward is used to isolate and cure COVID-19 patients with mild cases. It is normally not used for intensive care unit (ICU). Due to highly contagious of coronavirus, health care workers are not encouraged to stay in the COVID-19 inpatient ward for a long time. Hence, the additional presence of nurses and doctors are not considered in this study. The conclusion of this study is not applicable for ventilations in ICU cases. This would be the fourth limitation of the

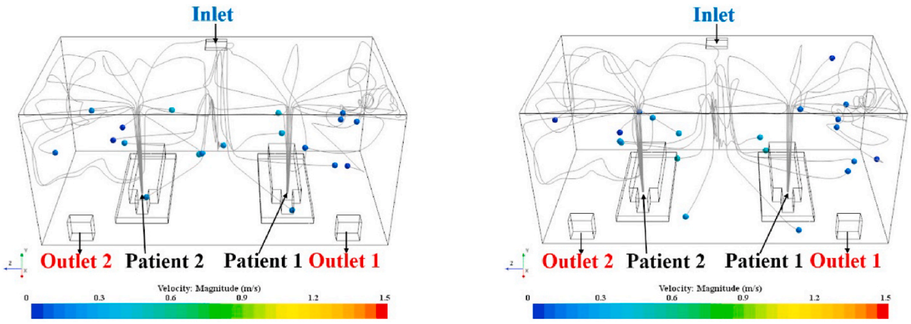

(a) Trajectories of 3 μm particles (b) Trajectories of 6 μm particles

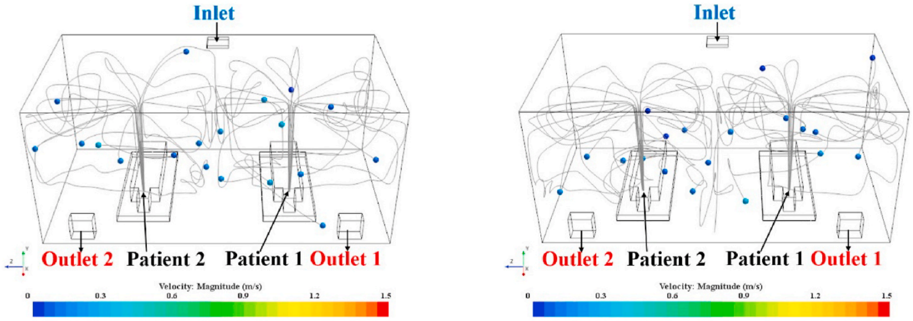

(c) Trajectories of 12 μm particles (d) Trajectories of 20 μm particles

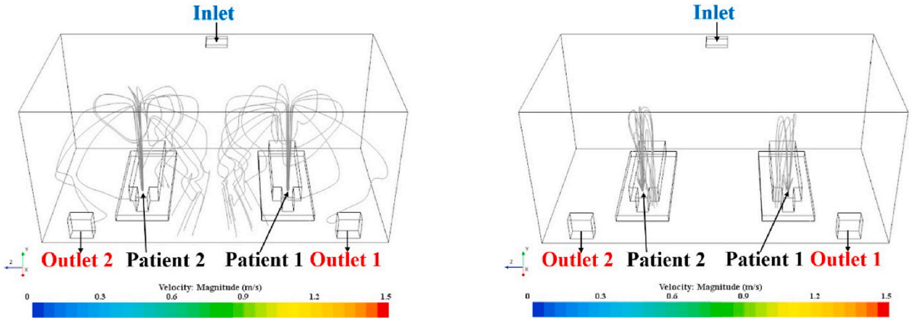

(e) Trajectories of 45 μm particles (f) Trajectories of 175 μm particles

Fig. 18. Particle trajectories in ventilation strategy III. When particle diameters are smaller than 20 μm, the particles follow the coughing jet flow to the ceiling and diffuse in all directions. When particle diameters are larger than 45 μm, the particles fall onto the bed, the outlet and the ground near the patients' heads.

Table 3
The fate of injected particles. This table summarizes the percentage of particles (in different diameters) suspended in the air and those removed by two major mechanisms, i.e., by ventilation through the exhaust outlet(s) and by deposition on different surfaces. (The three ventilation strategies have an identical air change rate of 12.3 h^{-1}.)

Ventilation strategy	Particle diameters (μm)	Manikins skin (%)	All beds (%)	Floor (%)	Ceiling and walls (%)	Exhaust (%)	Suspended in air (%)
I	3	0.2	0.3	3.4	2.3	88.7	5.1
	6	0.2	0.3	3.6	2.1	88.7	5.1
	12	0.2	0.3	4.2	1.9	88.5	4.9
	20	0.3	0.5	7.4	1.4	86.1	4.3
	45	7.5	13.4	70.6	0.2	7	1.3
	175	45.5	43.8	10.6	0	0	0.1
II	3	0.3	0.3	4.2	2.4	85.4	7.4
	6	0.3	0.3	4.7	2.1	85.3	7.3
	12	0.3	0.4	5.1	2	85	7.2
	20	0.4	0.5	7.9	1.6	83.4	6.2
	45	7.9	18.8	71.6	0.3	0	1.4
	175	43.2	46.9	9.8	0	0	0.1
III	3	0.4	0.4	3.1	2.5	67.3	26.3
	6	0.4	0.5	3.4	2.3	67.3	26.1
	12	0.5	0.6	4.4	2.1	67.1	25.3
	20	0.6	0.7	14.3	1.7	64.3	18.4
	45	3.1	16.3	60.6	0.3	18.1	1.6
	175	41	53.6	5.3	0	0	0.1

current study.

6. Conclusions

In this paper, a comparative study of three different ventilation strategies in a prefabricated double-patient ward has been provided. Three ventilation strategies have an identical air change rate of 12.3 h-^{1}. This air change rate satisfies the requirement (>12 h^{-1}) of COVID-19 inpatient wards [19]. Flow structures and the respiratory droplets and aerosols have been analysed and compared among the three ventilation strategies. The predicted fate of particles is listed and compared quantitatively in a table among the three ventilation strategies.

Ventilation strategy I has the inlet and outlet on the same sidewall. This kind of inlet-outlet layout forms a "U" type of structure which can include a large air motion in the ward. In ventilation strategy II, the inlet and the outlet are on the opposite sidewalls. The inlet-outlet flow in ventilation strategy II forms a "L" type shape which can drive the air motion directly in about half ward. The ventilation strategy III has one inlet on the ceiling and two outlets on the far sidewall. The inlet-outlet flow in ventilation strategy III is quite different from ventilation strategies I and II. It is from the ceiling to the ground and has little effect on the coughing jet flows.

In all the three ventilation strategies, the respiratory droplets and aerosols are sprayed in the coughing jet flows of two patients. When particle diameters are smaller than 20 μm, the particles can move along with the main flow structures. Most of them are removed by ventilation to the outlet(s), with 86.1–88.7% in ventilation strategy I, 83.4–85.4% in ventilation strategy II, and 64.3–67.3% in ventilation strategy III. In ventilation strategy III, because a large amount of stagnated air is located above the two patients, 18.4–26.3% of small particles are suspended in the air. In contrast, with the longest circuit of air in the prefabricated inpatient ward, ventilation strategy I has the best removal efficiency of small particles.

When particle diameters are larger than 45 μm, the respiratory droplets cannot move with the flow structures for a long path. Most of these large particles fall onto solid surfaces in different regions of the ward. In ventilation strategy I, the particles fall onto the solid surfaces near the patients' heads, the corridor between the two patients and the region near the outlet. In ventilation strategy II, the particles have fallen on the solid surfaces near the patients' head, the ground between the two patients and the region between patient 2 and the sidewall $z = 6$ m. In ventilation strategy III, the particles fall onto the bed, the outlet and the ground near the patients' heads. Hence, health workers should pay more attention to these contaminated areas. Targeted cleaning on the polluted areas is necessary in a prefabricated inpatient ward.

A correct layout of the outlet(s) can highly promote the removal of some large particles (e.g., 45 μm). In ventilation strategy II, the outlet is installed in the opposite direction of landing particles. None of the 45 μm particles are removed by the outlet. In ventilation strategy III, the outlets are installed in the landing area of large particles and close to the polluted source(s). Therefore, 18.1% of the 45 μm particles can be collected by the filtration systems and removed by the exhaust outlets.

Declaration of competing interest

We declare that we have no financial and personal relationships with other people or organizations that can inappropriately influence our work; there is no professional or other personal interest of any nature or kind in any product, service and/or company that could be construed as influencing the position presented in, or the review of, the manuscript entitled, "Numerical Study of Three Ventilation Strategies in a Prefabricated COVID-19 Inpatient Ward".

Acknowledgement

The authors are grateful for the support by the virtual simulation experiment teaching project of Chang 'an University and the fundamental research funds for the central universities, CHD (No. 310841151099).

References

[1] World Health Organization, Transmission of SARS-CoV-2: implications for infection prevention precautions. https://www.who.int/emergencies/diseases/novel-coronavirus-2019/technical-guidance, 9 July 2020.

[2] J. Liu, X. Liao, S. Qian, et al., Community transmission of severe acute respiratory syndrome coronavirus 2, Shenzhen, China, 2020, Emerg. Infect. Dis. (2020), https://doi.org/10.3201/eid2606.200239.

[3] J. Chan, S. Yuan, K. Kok, et al., A familial cluster of pneumonia associated with the 2019 novel coronavirus indicating person-to-person transmission: a study of a family cluster, Lancet (2020), https://doi.org/10.1016/S0140-6736(20)30154-9.

[4] Q. Li, X. Guan, P. Wu, et al., Early transmission dynamics in Wuhan, China, of novel coronavirus-infected pneumonia, N. Engl. J. Med. (2020), https://doi.org/10.1056/NEJMoa2001316.

[5] C. Huang, Y. Wang, X. Li, et al., Clinical features of patients infected with 2019 novel coronavirus in Wuhan, China, Lancet 395 (2020) 497–506.

[6] R.M. Burke, C.M. Midgley, A. Dratch, et al., Active monitoring of persons exposed to patients with confirmed COVID-19 — United States, January–February 2020, MMWR Morb. Mortal. Wkly. Rep. (2020), https://doi.org/10.15585/mmwr.mm6909e1external.iconv.

[7] J. Wang, G.Q. Du, COVID-19 may transmit through aerosol, Ir. J. Med. Sci. 189 (4) (2020) 1143–1144. Brief report.

[8] D.N. Van, D. Morris, T. Bushmaker, et al., Aerosol and surface stability of SARS-CoV-2 as compared with SARS-CoV-1, N. Engl. J. Med. (2020), https://doi.org/10.1056/NEJMc2004973.

[9] Y. Li, G.M. Leung, J.W. Tang, X. Yang, et al., Role of ventilation in airborne transmission of infectious agents in the built environment—a multidisciplinary systematic review, Indoor Air 17 (2007) 2–18.

[10] World Health Organization, WHO calls for healthy, safe and decent working conditions for all health workers, amidst COVID-19 pandemic. https://www.who.int/news-room/detail/28-04-2020-who-calls-for-healthy-safe-and-decent-working-conditions-for-all-health-workers-amidst-COVID-19-pandemic.

[11] C.Y.H. Chao, M.P. Wan, L. Morawska, et al., Characterization of expiration air jets and droplet size distribution immediately at the mouth opening, Aerosol. Sci. 40 (2009) 122–133.

[12] L. Bourouiba, E. Dehandschoewercker, J.W.M. Bush, Violent expiratory events: on coughing and sneezing, J. Fluid Mech. 745 (2014) 537–563.

[13] World Health Organization, Shortage of personal protective equipment endangering health workers worldwide. https://www.who.int/news-room/detail/03-03-2020-shortage-of-personal-protective-equipment-endangering-health-workers-worldwide.

[14] Z. Bolashikov, A. Melikov, W. Kierat, Z. Popiołek, M. Brand, Exposure of health care workers and occupants to coughed airborne pathogens in a double-bed hospital patient room with overhead mixing ventilation, HVAC R Res. 18 (2012) 602–615.

[15] J. Pantelic, K.W. Tham, Adequacy of air change rate as the sole indicator of an air distribution system's effectiveness to mitigate airborne infectious disease transmission caused by a cough release in the room with overhead mixing ventilation: a case study, HVAC R Res. 19 (2013) 947–961.

[16] U. Ghia, S. Konangi, A. Kishore, M. Gressel, et al., Assessment of health-care worker exposure to pandemic flu in hospital rooms, Build. Eng. 118 (1) (2012) 442–449.

[17] D. Licina, A. Melikov, J. Pantelic, et al., Human convection flow in spaces with and without ventilation: personal exposure to floor-released particles and cough-released droplets, Indoor Air 25 (2015) 672–682.

[18] F. Memarzadeh, W. Xu, Role of air changes per hour (ACH) in possible transmission of airborne infections, Build. Simulat. 5 (2012) 15–28.

[19] World Health Organization, Infection prevention and control during health care when novel coronavirus (nCoV) infection is suspected, 1-25, https://www.who.int/publications-detail/infection-prevention-and-control-during-health-care-when-novel-coronavirus-(ncov)-infection-is-suspected-20200125, 2020.

[20] Z.T. Ai, A.K. Melikov, Airborne spread of expiratory droplet nuclei between the occupants of indoor environments: a review, Indoor Air 28 (4) (2018) 500–524.

[21] W.B. Faulkner, F. Memarzadeh, G. Riskowski, et al., Effects of air exchange rate, particle size and injection place on particle concentrations within a reduced-scale room, Build. Environ. 92 (2015) 246–255.

[22] E.S. Mousavi, K.R. Grosskopf, Ventilation rates and airflow pathways in patient rooms: a case study of bio-aerosol containment and removal, Ann. Occup. Hyg. (2015) 1–10.

[23] A. Melikov, J. Kaczarczyk, Measurement and prediction of indoor air quality using a breathing thermal manikin, Indoor Air 17 (2007) 50–59.

[24] C.K.M. Poon, A.C.K. Lai, An experimental study quantifying pulmonary ventilation on inhalation of aerosol under steady and episodic emission, J. Hazard Mater. 192 (2011) 1299–1306.

[25] W. Liu, J. Wen, J. Chao, et al., Accurate and high-resolution boundary conditions and flow fields in the first-class cabin of an MD-82 commercial airliner, Atmos. Environ. 56 (2012) 33–44.

[26] W. Liu, T. Hooff, Y. An, et al., Modeling transient particle transport in transient indoor airflow by fast fluid dynamics with the Markov chain method, Build. Environ. 186 (2020), 107323.

[27] D.T. Bolster, P.F. Linden, Particle transport in low-energy ventilation systems. Part 2: transients and experiments, Indoor Air 19 (2009) 130–144.

[28] N. Zhang, Z. Zheng, S. Eckels, et al., Transient response of particle distribution in a chamber to transient particle injection, Part. Syst. Charact. 26 (2009) 199–209.

[29] P.L. Betts, I.H. Bokhari, Experiments on turbulent natural convection in an enclosed tall cavity, Int. J. Heat Fluid Flow 21 (2000) 675–683.

[30] D. Blay, S. Mergur, C. Niculae, Confined turbulent mixed convection in the presence of a horizontal buoyant wall jet, Fundamentals Mixed Convect., ASME HTD 213 (1992) 65–72.

[31] K. Ito, S. Kato, S. Murakami, Model experiment of flow and temperature field in room for validating numerical simulation analysis of newly proposed ventilation effectiveness, J. Architect., Plann. Environ. Eng. 534 (2000) 49–56 (In Japanese).

[32] S. Murakami, S. Kato, R. Yoshie, Measurement of turbulence statistics in a model fire room by LDV, Build. Eng. 101 (2) (1995) 287–301.

[33] M. Wang, Q.Y. Chen, Assessment of various turbulence models for transitional flows in an enclosed environment (RP-1271), HVAC R Res. 15 (6) (2009) 1099–1119.

[34] P.J. Roache, Verification and Validation in Computational Science and Engineering, Hermosa Publishers, Albuquerque, NM, 1998.

[35] Z. Zhai, Z. Zhang, W. Zhang, Q. Chen, Evaluation of various turbulence models in predicting airflow and turbulence in enclosed environments by CFD: part-1: summary of prevalent turbulence models, HVAC R Res. 13 (6) (2007).

[36] Z. Zhang, W. Zhang, Z. Zhai, Q. Chen, Evaluation of various turbulence models in predicting airflow and turbulence in enclosed environments by CFD: part-2: comparison with experimental data from literature, HVAC R Res. 13 (6) (2007).

[37] S. Gilani, H. Montazeri, B. Blocken, CFD simulation of stratified indoor environment in displacement ventilation: validation and sensitivity analysis, Build. Environ. 95 (2016) 299–313.

[38] C. Buratti, D. Palladino, E. Moretti, Prediction of indoor conditions and thermal comfort using CFD simulations: a case study based on experimental data, Energy Procedia 126 (2017) 115–122.

[39] Z. Shi, J. Chen, R. You, C. Chen, Q. Chen, Modeling of gasper-induced jet flow and its impact on cabin air quality, Energy Build. 127 (2016) 700–713.

[40] B.P.P. Barbosa, N.D.C.L. Brum, Validation and assessment of the CFD-0 module of CONTAM software for airborne contaminant transport simulation in laboratory and hospital applications, Build. Environ. 142 (2018) 139–152.

[41] H.T. Van, B. Blocken, CFD simulations of mixing ventilation at low Reynolds numbers: effect of spatial discretization scheme, July 3-8, in: 14th International Conference on Indoor Air Quality and Climate (Indoor Air 2016), 2016. Ghent, Belgium.

[42] S. Sadrizadeh, A. Ploskic, On the boundary conditions of numerical particle simulation in indoor environment, in: Proc. 14th Int. Conf. Indoor Air Qual. Clim, 2016.

[43] A.C. Rai, C.H. Lin, Q. Chen, Numerical modeling of volatile organic compound emissions from ozone reactions with human-worn clothing in an aircraft cabin, HVAC R Res. 20 (8) (2014) 922–931.

[44] C. Chen, B. Zhao, A modified Brownian force for ultrafine particle penetration through building crack modeling, Atmos. Environ. 170 (2017) 143–148.

[45] P.V. Nielsen, F.V. Winther, M. Buus, M. Thilageswaran, Contaminant flow in the microenvironment between people under different ventilation conditions, ASHRAE Trans. (2008) 632–640.

[46] I. Olmedo, P.V. Nielsen, M.R.D. Adana, R.L. Jensen, P. Grzelecki, Distribution of exhaled contaminants and personal exposure in a room using three different air distribution strategies, Indoor Air 22 (1) (2012) 64–76.

[47] N. Gao, J. Niu, Modeling particle dispersion and deposition in indoor environments, Atmos. Environ. 41 (2007) 386–396.

[48] A.C.K. Lai, L. Wang, F.Z. Chen, Experimental and numerical study on particle distribution in a two-zone chamber, Atmos. Environ. 42 (2008) 1717–1726.

[49] C. Chen, W. Liu, C.-H. Lin, Q. Chen, Comparing the Markov chain model with the eulerian and Lagrangian models for indoor transient particle transport simulations, Aerosol. Sci. Technol. 49 (2015) 857–871.

[50] H. Brohus, K.D. Balling, D. Jeppesen, Influence of movements on contaminant transport in an operating room, Indoor Air 16 (2006) 356–372.

[51] S. Mazumdar, Y. Yin, A. Guity, P. Marmion, B. Gulick, Q. Chen, Impact of moving objects on contaminant concentration distributions in an inpatient ward with displacement ventilation, HVAC R Res. 16 (5) (2010) 545–564.

[52] K.W.D. Cheong, S.Y. Phua, Development of ventilation design strategy for effective removal of pollutant in the isolation room of a hospital, Build. Environ. 41 (2006) 1161–1170.

[53] M.K. Satheesan, K.W. Mui, L.T. Wong, A numerical study of ventilation strategies for infection risk mitigation in general inpatient wards, Build. Simulat. 13 (1) (2020) 887–896.

[54] C.Y.H. Chao, M.P. Wan, A study of the dispersion of expiratory aerosols in unidirectional downward and ceiling-return type airflows using a multiphase approach, Indoor Air 16 (2006) 296–312.

[55] OpenFOAM v1906. OpenCFD-OpenFOAM-Official home of the open source computational fluid dynamics (CFD) toolbox. https://www.openfoam.com/, 2019.

[56] H.P. Zhu, Z.Y. Zhou, R.Y. Yang, A.B. Yu, Discrete particle simulation of particulate systems: theoretical developments, Chem. Eng. Sci. 62 (2007) 3378–3396.

[57] C.T. Crowe, M. Sommerfeld, Y. Tsuji, Multiphase Flows with Droplets and Particles, second ed., CRC Press., Boca Raton,Florida, USA, 1998.

[58] S. Balachandar, A scaling analysis for point–particle approaches to turbulent multiphase flows, Int. J. Multiphas. Flow 35 (9) (2009) 801–810.

[60] J.K. Gupta, C.H. Lin, Q. Chen, Flow dynamics and characterization of a cough, Indoor Air 19 (2009) 517–525.

[61] H. Qian, Y. Li, Removal of exhaled particles by ventilation and deposition in a multi-bed airborne infection isolation room, Indoor Air 20 (2010) 284–297.

[62] P.V. Nielsen, Y. Li, M. Buus, et al., Risk of cross-infection in a hospital ward with downward ventilation, Build. Environ. 45 (2010) 2008–2014.